World Electric Vehicle Journal

MDPI

Article

SMO-Residual-Driven Event-Triggered Sensorless FCS-MPC for PMSM Drives

Zhiwang Xing [1], Xipei Ma [1,*], Yansong Wang [1], Pingqing Fan [1], Huankang Zhang [1] and Yang Gao [2]

[1] School of Mechanical and Automotive Engineering, Shanghai University of Engineering Science, Shanghai 201620, China; xingzwx@163.com (Z.X.); wysgcd@sues.edu.cn (Y.W.); fpq@sues.edu.cn (P.F.); 15061160933@163.com (H.Z.)

[2] Shanghai Kehai Huatai Marine Electrical Co., Ltd., Shanghai 201601, China; weihaoyunshigy@163.com

* Correspondence: maxipei@sues.edu.cn

Abstract

Periodic sensorless finite-control-set model predictive control (FCS-MPC) evaluates all eight voltage vectors every 10 µs, even when the applied vector is still adequate. This study develops a controller that reuses the applied vector when one held-vector prediction satisfies the descent and current constraints. A double-power saturated sliding-mode observer supplies position and speed, and its sliding residual tightens or relaxes the descent threshold. Under bounded lumped disturbances, the sliding error reaches a prescribed boundary layer in bounded time, while the compensated-current error remains locally uniformly ultimately bounded. At the largest simulated initial error, the double-power law shortens boundary-layer entrance from 2.11 to 1.08 ms and post-load-step speed-estimation recovery from 55.23 to 24.35 ms. Across the composite profile, 39.42% of periods require full enumeration, reducing candidate-state checks by 60.6%. With a similar update budget, position RMSE falls from 1.035° to 0.949°. On the hardware bench, full-enumeration checks fall by 21.6% and equivalent switching frequency by 14.9%; speed-tracking and electrical-angle RMSE increase by 1.22 r/min and 0.400°, respectively. These measurements show the computational saving and its accuracy cost.

Keywords: permanent-magnet synchronous motor; sensorless control; finite-control-set model predictive control; sliding-mode observer; double-power reaching law; adaptive event triggering

Check for updates

Academic Editor: Peter Van den Bossche

Received: 12 October 2026
Revised: 4 November 2026
Accepted: 10 November 2026
Published: 12 November 2026

Copyright: © 2026 by the authors. Published by MDPI on behalf of the World Electric Vehicle Association. Licensee MDPI, Basel, Switzerland. This article is an open access article distributed under the terms and conditions of the Creative Commons Attribution (CC BY) license.

1. Introduction

Permanent-magnet synchronous motors (PMSMs) combine high efficiency with fast dynamic response and are widely used in servo drives, robotics, and electric-transportation auxiliary systems. Finite-control-set model predictive control (FCS-MPC) evaluates inverter switching states directly and can include current constraints and switching penalties [1–3]. Recent work improves the prediction model, identifies parameters online, or reduces the work performed in each optimization [4–9]. Most implementations still optimize at every sample. Mechanical position sensors add cost, wiring, and packaging constraints and create another failure point. Compact auxiliary drives can avoid this hardware through sensorless control. The unresolved computational question is when the predictive controller actually needs a new candidate search.

Automotive electric coolant pumps are important actuators in vehicle thermal-management systems, where variable-speed electric drives regulate coolant flow in re-

sponse to changing thermal demands. The low-voltage surface-mounted PMSM configuration considered in this study provides a potential platform for applying sensorless predictive control to this class of auxiliary drives.

Back-electromotive-force (back-EMF) sliding-mode observers (SMOs) are compact and robust to matched disturbances, which makes them useful in medium- and high-speed sensorless PMSM drives. Recent designs use barrier functions, super-twisting terms, discrete-domain control, frequency-locked loops, flux observation, or low-speed voltage injection [10–14]. Ref. [15] combines an adaptive SMO with separate disturbance-observer feedforward compensation, while Ref. [16] identifies temperature-dependent electrical parameters online. The proposed controller uses a different signal from the observer: the sliding residual decides when FCS-MPC searches the candidate set. Continuous injection is used near the sliding surface, where parameter mismatch and inverter nonidealities appear in the same bounded channel as the back-EMF. The observer is tuned for rapid recovery from a large error and continued correction inside the boundary layer. Accordingly, the analysis treats the recovered back-EMF as a bounded-disturbance reconstruction inside the boundary layer, with a finite residual in place of exact recovery.

Reaching laws, terminal sliding modes, and higher-order sliding modes provide theoretical foundations for this problem [17–19]; related methods have recently been applied to finite-time observation and fast robust control of PMSM drives [20]. The settling time of a finite-time stable system generally depends on its initial condition, whereas fixed-time stability admits a uniform initial-condition-independent upper bound [21,22]. For an SMO with saturated injection under bounded lumped disturbances, the analysis establishes entrance into and retention within a computable boundary layer. Incorporating the complementary effects of different powers far from and near the sliding surface into a back-EMF SMO requires a unified analysis of the disturbance bound, dimensional normalization, and saturation within the boundary layer in the PMSM error dynamics.

Event-triggered control determines when to update a control task through a state-dependent condition, providing a framework for reducing redundant periodic computation [23,24]. A finite-time observer has also been incorporated into model-based event-triggered control to improve update decisions from reconstructed states [25]. Event-triggering has been extended to robust MPC and disturbance-observer-compensated nonlinear MPC, with analyses of asymptotic bounds and average sampling rates [26,27]. For power converters, prescribed state thresholds have been used to hold the control action between events and reduce repeated FCS-MPC optimization and switching [28]. Event-triggered robust MPC combined with an extended-state observer can further reduce computation under model uncertainty [29]. Existing thresholds are mainly formed from plant states, prediction errors, or disturbance estimates. The sliding residual provides an additional observation-reliability signal: its growth indicates departure from the sliding surface and calls for denser candidate evaluation. Here, the event decision is evaluated at each discrete sampling instant through one-step descent and constraint feasibility under the held vector.

Shen et al. [30] use an SMO to estimate load torque for feedforward compensation; rotor position is measured, and the event condition comes from a reconstructed PMSM model. Ref. [15] focuses on adaptive sensorless observation, while Refs. [7,16] correct electrical-parameter errors online. Inverse-model reference-model learning has also been applied to adaptive fuzzy DC-motor speed control under changing loads [31]. In the proposed controller, the back-EMF SMO supplies position and speed, and its sliding residual is also the input to the event rule. A larger residual tightens the descent test and makes a new candidate search more likely, so the observer and trigger are tuned as one control loop. Table 1 summarizes these distinctions.

Table 1. Positioning of the proposed method relative to closely related PMSM control approaches.

Approach	Main Role	Relation to the Present Work
Jin et al. [15]	Adaptive SMO and separate disturbance feedforward compensation	Observer and candidate scheduler are separate layers.
Shen et al. [30]	Load-torque SMO and model-derived event condition	Model-derived trigger with measured rotor position.
Refs. [7,16]	Online parameter rectification or identification	Parameter-robustness layer for predictive control.
Present work	Back-EMF SMO with residual-adaptive FCS-MPC	The SMO residual directly schedules candidate enumeration.

The main contribution is an event rule driven directly by the SMO residual: a rising residual tightens the one-step descent test and makes candidate enumeration more likely. The back-EMF observer uses a double-power saturated reaching law, for which a uniform bound is derived on entrance into a prescribed boundary layer under bounded disturbances. A local uniform-ultimate bound is also established for the compensated-current error. Simulations and hardware tests report the resulting changes in candidate evaluations, execution time, switching activity, and estimation accuracy.

2. Materials and Methods

2.1. PMSM Model and Problem Formulation

The standard surface-mounted PMSM voltage model and finite-control-set prediction framework in Equations (1)–(8) follow established PMSM FCS-MPC formulations [1–3]. The coordinate transformation, delay compensation, and notation used in this study are specified below.

2.1.1. Stationary-Frame Model and Lumped Disturbance

For a surface-mounted PMSM, neglecting magnetic saturation and core loss in the nominal model, the stationary α–β voltage equation is

$$\dot{\boldsymbol{i}}_{\alpha\beta} = -a_0 \boldsymbol{i}_{\alpha\beta} + b_0 \boldsymbol{u}_{\alpha\beta} - \boldsymbol{d}_{\alpha\beta} \tag{1}$$

where $\boldsymbol{i}_{\alpha\beta} = [i_\alpha, i_\beta]^{\mathrm{T}}$, $\boldsymbol{u}_{\alpha\beta} = [u_\alpha, u_\beta]^{\mathrm{T}}$, $a_0 = R_{s0}/L_{s0}$, and $b_0 = 1/L_{s0}$. Back-EMF $\boldsymbol{e}_{\alpha\beta}$, parameter mismatch, and inverter nonidealities are combined into the lumped disturbance $\boldsymbol{d}_{\alpha\beta}$:

$$\begin{aligned} \boldsymbol{d}_{\alpha\beta} &= \frac{\boldsymbol{e}_{\alpha\beta}}{L_{s0}} + \boldsymbol{w}_p, \\ \boldsymbol{e}_{\alpha\beta} &= \psi_f \omega_e [\cos\theta_e,\ \sin\theta_e]^{\mathrm{T}}. \end{aligned} \tag{2}$$

The lumped disturbance combines the back-EMF-related term with parameter mismatch and inverter nonidealities in the observer-injection channel. On a bounded operating domain, its uniform envelope follows from $\psi_f|\omega_e|$ and the corresponding mismatch bounds. The electrical-angle phase origin follows the adopted Clarke–Park convention.

The following assumptions support the analysis.

Assumption 1. *Within a compact operating domain Ω, let $\omega_b = \max(|\hat{\omega}_e|, 100)$. The lumped disturbance satisfies $\|\boldsymbol{d}_{\alpha\beta}\|_\infty \le \psi_f \omega_b / L_s + \bar{w}_p$, where $\bar{w}_p = 3000\,\mathrm{A/s}$ is a conservative upper bound for the residual terms over the tested experimental operating range. These terms include parameter mismatch, inverter nonidealities, and the back-EMF mismatch caused by the bounded*

speed-estimation error. Voltage and speed commands are bounded, and the actuation delay does not exceed one control period.

Assumption 2. *Closed-loop analysis considers an observable forward-rotation region with* $\omega_e \geq \omega_{\min} > 0$ *and a locked PLL.*

Assumptions 1 and 2 define the operating domain of the back-EMF-based observer. In the implementation, the trigger is enabled only after PLL locking, and loss of lock forces full candidate enumeration.

2.1.2. Discrete FCS-MPC Prediction Model

Define the coordinate transformation $R(\theta_e) = \begin{bmatrix} \sin\theta_e & -\cos\theta_e \\ \cos\theta_e & \sin\theta_e \end{bmatrix}$, $\boldsymbol{x} = \boldsymbol{i}_{dq} = R(\theta_e)\boldsymbol{i}_{\alpha\beta}$, and $\boldsymbol{u} = \boldsymbol{u}_{dq} = R(\theta_e)\boldsymbol{u}_{\alpha\beta}$. This convention gives $R(\theta_e)\boldsymbol{e}_{\alpha\beta} = [0, \psi_f\omega_e]^{\mathrm{T}}$ and $\dot{R}R^{\mathrm{T}} = \omega_e J$. Thus, $\dot{\boldsymbol{x}} = \dot{R}\boldsymbol{i}_{\alpha\beta} + R\dot{\boldsymbol{i}}_{\alpha\beta}$ yields the dq-frame model:

$$\dot{\boldsymbol{x}} = (-a_0 I_2 + \omega_e J)\boldsymbol{x} + b_0\boldsymbol{u} + \boldsymbol{g}(\omega_e) + \boldsymbol{w}_d \tag{3}$$

$$J = \begin{bmatrix} 0 & 1 \\ -1 & 0 \end{bmatrix}, \qquad \boldsymbol{g}(\omega_e) = \begin{bmatrix} 0 & -\psi_f\omega_e/L_{s0} \end{bmatrix}^{\mathrm{T}} \tag{4}$$

Here, $\boldsymbol{w}_d$ is the equivalent lumped disturbance in the dq frame. Applying zero-order hold and forward-Euler discretization with control period T_s gives the following time-varying matrices:

$$\begin{aligned} A_k &= I_2 + T_s(-a_0 I_2 + \hat{\omega}_{e,k} J), \quad B = T_s b_0 I_2, \\ \boldsymbol{c}_k &= T_s \begin{bmatrix} 0 & -\psi_f\hat{\omega}_{e,k}/L_{s0} \end{bmatrix}^{\mathrm{T}}. \end{aligned} \tag{5}$$

Using the estimated speed gives

$$\boldsymbol{x}_{k+1} = A_k\boldsymbol{x}_k + B\boldsymbol{u}_k + \boldsymbol{c}_k + \boldsymbol{w}_k \tag{6}$$

With a one-sample digital control delay, the optimization result computed at instant k is applied from instant $k+1$. The currently applied vector $\boldsymbol{u}_{k-1}$ is used for the first delay-compensating prediction, followed by a second prediction for each candidate $\boldsymbol{v} \in \mathcal{U}$:

$$\begin{aligned} \hat{\boldsymbol{x}}_{k+1|k} &= A_k\hat{\boldsymbol{x}}_k + B\boldsymbol{u}_{k-1} + \boldsymbol{c}_k, \\ \hat{\boldsymbol{x}}_{k+2|k}(\boldsymbol{v}) &= A_{k+1}\hat{\boldsymbol{x}}_{k+1|k} + B\boldsymbol{v} + \boldsymbol{c}_{k+1}. \end{aligned} \tag{7}$$

If speed variation within one control period is negligible, $A_{k+1} \approx A_k$ and $\boldsymbol{c}_{k+1} \approx \boldsymbol{c}_k$ may be used. Otherwise, A_{k+1} and $\boldsymbol{c}_{k+1}$ should be updated using an extrapolated $\hat{\omega}_{e,k}$. The current reference is likewise extrapolated to $\boldsymbol{x}^*_{k+2}$ so that its time index matches the predicted state. A representative cost function is

$$J_k(\boldsymbol{v}) = \left\| \hat{\boldsymbol{x}}_{k+2|k}(\boldsymbol{v}) - \boldsymbol{x}^*_{k+2} \right\|^2_Q + \lambda_{\mathrm{sw}} \| S(\boldsymbol{v}) - S(\boldsymbol{u}_{k-1}) \|_1 + J_c(\boldsymbol{v}) \tag{8}$$

For any $W \succ 0$, define $\|\boldsymbol{\xi}\|^2_W = \boldsymbol{\xi}^{\mathrm{T}} W \boldsymbol{\xi}$; Equation (8) uses $W = Q$. The first term penalizes current-tracking error. The three upper-switch states associated with $\boldsymbol{v}$ are $S(\boldsymbol{v}) \in \{0,1\}^3$, and the second term penalizes switch transitions through their Hamming distance. The candidate set $\mathcal{U}$ contains six active vectors and two zero-voltage vectors with distinct switching states, for eight states in total. The constraint penalty $J_c(\boldsymbol{v})$ is zero for a state satisfying the predicted-current limit and $+\infty$ otherwise. The finite voltage set

and measured DC-bus voltage account for the voltage limit. If all eight states violate the predicted-current limit, a protective zero-vector fallback is used. The periodic baseline enumerates feasible states at every sample; the event mechanism only determines whether enumeration is repeated.

2.2. Proposed Control Strategy

2.2.1. Double-Power Saturated Sliding-Mode Observer

Equations (9)–(16) give the observer and practical fixed-time convergence derivation developed in this study.

Observer and Reaching Law

Define the current-estimation error $\boldsymbol{s} = \hat{\boldsymbol{i}}_{\alpha\beta} - \boldsymbol{i}_{\alpha\beta}$. To avoid raising a dimensional current directly to a fractional power, choose the normalization base $I_N = I_b = 7.8\,\mathrm{A}$ and define the dimensionless error $\boldsymbol{\sigma} = \boldsymbol{s}/I_N$. The dimensionless boundary-layer width is $\varphi \in (0,1)$, corresponding to a physical current width of $I_N\varphi$. The observer is

$$\dot{\hat{\boldsymbol{i}}}_{\alpha\beta} = -a_0\hat{\boldsymbol{i}}_{\alpha\beta} + b_0\boldsymbol{u}_{\alpha\beta} - \boldsymbol{\Phi}(\boldsymbol{\sigma}) \tag{9}$$

$$\Phi_j(\sigma_j) = \left(k_0(t) + k_1|\sigma_j|^p + k_2|\sigma_j|^q\right)\mathrm{sat}\left(\frac{\sigma_j}{\varphi}\right), \qquad j \in \{\alpha,\beta\} \tag{10}$$

Here, $0 < p < 1 < q$, and $k_0(t)$, k_1, and k_2 all have units of A/s. Equation (10) is defined componentwise, avoiding ambiguity between scalar and vector terms. The gain $k_0(t)$ provides a robustness margin against the lumped disturbance. The lower-power term maintains corrective action under small errors, whereas the higher-power term dominates under large errors and shortens the reaching time from large initial conditions. Compared with a constant-gain saturated reaching law, the structure adjusts its convergence gain with error magnitude. The higher-power term avoids the slow large-error response of a lower-power-only law, while the lower-power term prevents rapid loss of corrective action near the sliding surface. This complementary behavior is central to the proposed observer design. Subtracting the plant equation from the observer equation gives the componentwise error dynamics.

Let $\kappa_0(t) = k_0(t)/I_N$, $\kappa_1 = k_1/I_N$, $\kappa_2 = k_2/I_N$, and $\boldsymbol{d}_\sigma = \boldsymbol{d}_{\alpha\beta}/I_N$. Define the operating-domain gain margin as $\eta_0 = \inf_{t\geq 0}\{\kappa_0(t) - \|\boldsymbol{d}_\sigma(t)\|_\infty\}$. For the implemented schedule $k_0 = 1.8\psi_f\omega_b/L_s + 3000\,\mathrm{A/s}$, Assumption 1 gives $\eta_0 \geq 0.8\psi_f\omega_b/(L_sI_N)$. With $\psi_f = 0.0070\,\mathrm{Wb}$, $L_s = 0.45\,\mathrm{mH}$, $I_N = 7.8\,\mathrm{A}$, and $\omega_b \geq 100\,\mathrm{rad/s}$, the minimum normalized margin is $159.5\,\mathrm{s}^{-1} > 0$. Each component σ_j then satisfies the normalized error dynamics

$$\dot{\sigma}_j = -a_0\sigma_j - \left(\kappa_0(t) + \kappa_1|\sigma_j|^p + \kappa_2|\sigma_j|^q\right)\mathrm{sat}\left(\frac{\sigma_j}{\varphi}\right) + d_{\sigma,j} \tag{11}$$

Practical Fixed-Time Convergence

The analysis begins with an individual error component and then extends the result to the vector. Assume that the scheduled gain maintains a positive pointwise margin, $\eta_0 > 0$, and let $0 < \varphi < 1$.

Lemma 1. *If $\eta_0 > 0$, the set $\mathcal{S}_\varphi = \{\boldsymbol{\sigma} : \|\boldsymbol{\sigma}\|_\infty \leq \varphi\}$ is positively invariant.*

Proof. Consider the upper-right Dini derivative of any component at the boundary $\sigma_j = \varphi$. At this point $\mathrm{sat}(\sigma_j/\varphi) = 1$. Equation (11) and the definition of η_0 give

$$D^+\sigma_j \leq -a_0\varphi - \eta_0 - \kappa_1\varphi^p - \kappa_2\varphi^q < 0 \tag{12}$$

Similarly, $D^+\sigma_j > 0$ at $\sigma_j = -\varphi$. The vector field points inward on every face of the hyperrectangle $\mathcal{S}_\varphi$, proving positive invariance. □

Theorem 1. *Suppose Assumption 1 holds, $0 < p < 1 < q$, $0 < \varphi < 1$, and $\eta_0 > 0$. For any initial condition within the operating domain covered by Assumption 1, $\boldsymbol{\sigma}$ enters $\mathcal{S}_\varphi$ within a uniform time bound independent of the initial condition. The reaching time satisfies*

$$T_\varphi \le \frac{1}{\kappa_2(q-1)} + \frac{1-\varphi^{1-p}}{\kappa_1(1-p)} \tag{13}$$

Proof. For component j, set $V_j = |\sigma_j|$. When $V_j > \varphi$, $\mathrm{sat}(\sigma_j/\varphi) = \mathrm{sgn}(\sigma_j)$. Applying $D^+|\sigma_j| = \mathrm{sgn}(\sigma_j)\dot{\sigma}_j$, $-a_0 V_j \le 0$, and $\mathrm{sgn}(\sigma_j) d_{\sigma,j} \le \|\boldsymbol{d}_\sigma\|_\infty$, the definition of η_0 gives

$$\begin{aligned} D^+ V_j &\le -a_0 V_j - \eta_0 - \kappa_1 V_j^p - \kappa_2 V_j^q, \\ &\le -\kappa_1 V_j^p - \kappa_2 V_j^q. \end{aligned} \tag{14}$$

In the first stage, $V_j \ge 1$ and $D^+ V_j \le -\kappa_2 V_j^q$ even if only the higher-power term is retained. The time $T_{j,1}$ for V_j to decrease from any $V_j(0) \ge 1$ to 1 is bounded by separation of variables:

$$T_{j,1} \le \int_1^{V_j(0)} \frac{\mathrm{d}V}{\kappa_2 V^q} = \frac{1 - V_j(0)^{1-q}}{\kappa_2(q-1)} \tag{15}$$

Because $q > 1$ and $V_j(0) \ge 1$, the first-stage time has the uniform bound $1/[\kappa_2(q-1)]$.

In the second stage, $\varphi < V_j \le 1$ and $D^+ V_j \le -\kappa_1 V_j^p$ when only the lower-power term is retained. Integrating from 1 to φ gives

$$T_{j,2} \le \int_\varphi^1 \frac{\mathrm{d}V}{\kappa_1 V^p} = \frac{1-\varphi^{1-p}}{\kappa_1(1-p)} \tag{16}$$

Adding the two stages yields $T_j \le T_{j,1} + T_{j,2}$. Because this bound contains no $V_j(0)$, it is uniform. If the initial condition is already in the second stage or inside $\mathcal{S}_\varphi$, the omitted stage takes zero time and the bound remains conservative. The time for the two-dimensional error vector to enter $\mathcal{S}_\varphi$ is the maximum of the two componentwise times and still satisfies Equation (13). Lemma 1 guarantees that the vector remains in the set afterward. □

Inside the boundary layer, the residual level is governed by φ, quantization noise, and switching ripple. Decreasing φ tightens the theoretical residual while increasing noise sensitivity. The resulting property is practical fixed-time entrance into an adjustable boundary layer.

Parameter selection follows a constraint-first procedure. First, k_0 is scheduled to maintain $\eta_0 > 0$ over the operating range. Next, k_2 is increased until the large-error approach is sufficiently fast, whereas k_1 is refined for motion near the boundary layer. Finally, φ is chosen above the measured noise and ripple floor; reducing it further improves the nominal residual bound but amplifies chattering. The resulting values are locally checked by the sensitivity study in Section 3.1.2.

The equivalent injection is low-pass-filtered and scaled by the nominal inductance to form a back-EMF estimate; parameter mismatch and inverter nonidealities within the lumped disturbance introduce estimation bias. Position and speed are obtained from a type-II PLL using atan2 phase detection. The estimation error can be treated as bounded only when the back-EMF amplitude is sufficient and the unsaturated PLL remains within its local locking region. The locked-PLL condition in Assumption 2 refers to these requirements.

2.2.2. Residual-Adaptive Event-Triggered FCS-MPC

Equations (17)–(42) are derived in this study from the discrete PMSM prediction model, the proposed residual-adaptive trigger, and the associated Lyapunov analysis.

Overall Architecture

In Figure 1, the feedback module combines voltage reconstruction, the SMO, and the PLL. Voltage is reconstructed from S_k and U_{dc}. Measured current $\boldsymbol{i}_{\alpha\beta}$ feeds the SMO directly and is forwarded to FCS-MPC with the PLL angle and speed estimates and the SMO residual. The speed estimate closes the outer loop, while the residual adjusts the threshold for enumeration or vector holding.

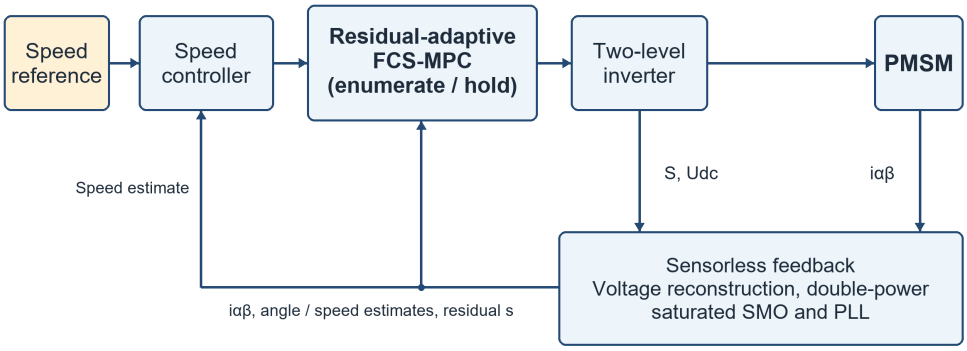


Figure 1. Overall architecture of the proposed sensorless adaptive event-triggered FCS-MPC scheme.

Figure 2 shows the order of execution in one control period. The SMO and PLL are updated every period. If PLL locking fails, full enumeration is forced. Otherwise, the held vector is tested for predicted descent, current-limit feasibility, and maximum hold duration. If no trigger is generated, the most recently selected vector is held. If a trigger occurs, the feasible candidates are enumerated; a protective zero vector is used if none is feasible. After either branch, the next adaptive threshold is updated and the switching state is applied.

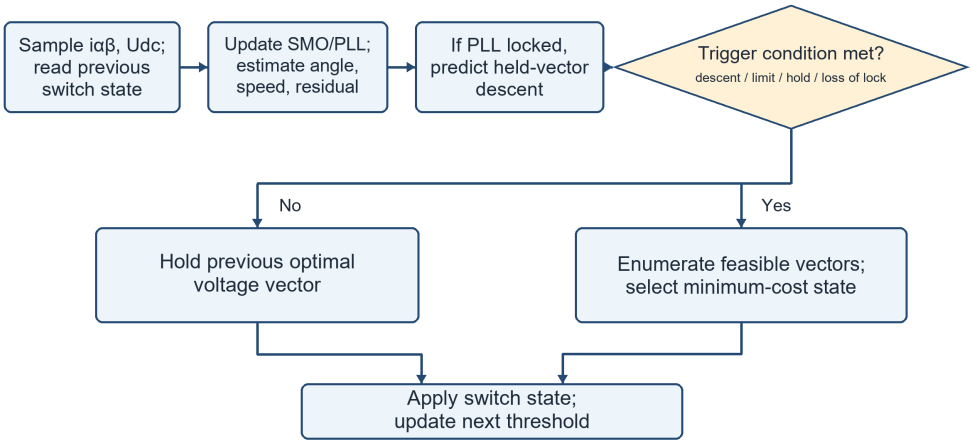


Figure 2. Per-period execution flow of the adaptive event-triggered FCS-MPC scheme.

Let N denote the number of control periods, N_e the number of periods with full enumeration, and $r_e = N_e/N$. Periodic FCS-MPC evaluates $8N$ candidate vectors. Counting one held-vector prediction separately in every period, the adaptive branch performs $N + 8N_e$ prediction evaluations, giving the normalized branch-level prediction workload:

$$\frac{N + 8N_e}{8N} = \frac{1}{8} + r_e.$$

The event mechanism adds one held-vector prediction, a first-order threshold update, scalar comparisons, and a hold counter while using the existing sensing and power hardware.

One-Step Descent Prediction Under the Held Vector

Choose the discrete Lyapunov candidate $V(z_k) = z_k^{\mathrm{T}} P z_k$, with $P = P^{\mathrm{T}} \succ 0$. The one-sample actuation delay is described in Section 2.1.2. At decision instant k, the vector u_{k-1} still applied first produces $\hat{x}_{k+1|k}$. Define the compensated-error sequence $z_k = \hat{x}_{k+1|k} - x^*_{k+1}$. The subscript of z_k denotes the decision instant, whereas the predicted physical state corresponds to $k+1$. Let k_j be the most recent event instant. If the previously optimal vector $u^*_{k_j}$ is held for another sample, the state prediction at $k+2$, matching the horizon used for candidate optimization, is

$$\hat{x}^h_{k+2|k} = A_{k+1}\hat{x}_{k+1|k} + Bu^*_{k_j} + c_{k+1} \tag{17}$$

Using the corresponding reference x^*_{k+2}, define the one-step error prediction under the held vector and its nominal Lyapunov increment as

$$\begin{aligned} \hat{z}^h_{k+1|k} &= \hat{x}^h_{k+2|k} - x^*_{k+2}, \\ \Delta V^h_k &= V(\hat{z}^h_{k+1|k}) - V(z_k). \end{aligned} \tag{18}$$

Calculating ΔV^h_k requires one prediction under the held vector. One-step descent refers to evolution of the compensated-error sequence from z_k to z_{k+1}, corresponding to the physical prediction horizon advancing from $k+1$ to $k+2$. This keeps the compensated state sequence aligned with the two-step cost function. Predicted descent below the required margin triggers re-enumeration; the no-event condition is

$$\Delta V^h_k \le -\alpha \|z_k\|^2 + \delta_k \tag{19}$$

Here, $\alpha > 0$ specifies the desired descent rate and $\delta_k \ge 0$ is the permitted descent relaxation. The units of δ_k match those of the Lyapunov increment; when $P = I_2$, they are A^2. Reducing δ_k lowers the right-hand side, making the held vector less likely to satisfy the inequality and increasing the event frequency. Accounting for hard constraints and a finite hold duration, define the trigger variable Γ_k by

$$\Gamma_k = 1 \Longleftrightarrow \left[\Delta V^h_k > -\alpha \|z_k\|^2 + \delta_k\right] \vee C^h_k \vee [k - k_j \ge N_{\max}] \tag{20}$$

In the implementation, the Boolean condition C^h_k indicates that the magnitude of the $k+2$ predicted current under the held vector exceeds 7.8 A. States exceeding this limit are also excluded during candidate enumeration. When $\Gamma_k = 1$, enumeration is repeated; when $\Gamma_k = 0$, the previous switching state is held. A maximum hold count of $N_{\max} = 40$ forces re-evaluation under the adopted counting convention, so the discrete inter-event interval does not exceed $N_{\max} T_s$.

Nominal predicted descent must next be related to actual descent. Define the one-step prediction error $r_k = z_{k+1} - \hat{z}^h_{k+1|k}$. It mainly comprises state-observation error, accumulated discrete-model disturbance, and reference-extrapolation mismatch, with uniform bounds $\bar{\varepsilon}_o$, $\bar{w}$, and $\Delta\bar{x}^*$, respectively. Let the corresponding induced gains on the compact operating domain be g_e, g_w, and g_r. Then, a uniform constant $\bar{r}$ exists such that

$$\|r_k\| \le g_e\bar{\varepsilon}_o + g_w\bar{w} + g_r\Delta\bar{x}^* = \bar{r} \tag{21}$$

Define the actual one-step increment $\Delta V_k = V(\boldsymbol{z}_{k+1}) - V(\boldsymbol{z}_k)$. By the definition of $\boldsymbol{r}_k$,

$$\boldsymbol{z}_{k+1} = \hat{\boldsymbol{z}}^h_{k+1|k} + \boldsymbol{r}_k \tag{22}$$

$$\Delta V_k = \Delta V^h_k + 2(\hat{\boldsymbol{z}}^h_{k+1|k})^{\mathrm{T}} P \boldsymbol{r}_k + \boldsymbol{r}_k^{\mathrm{T}} P \boldsymbol{r}_k \tag{23}$$

Within the compact local analysis domain Ω_z specified in Assumption 3 below, suppose the nominal predicted error under the held vector satisfies $\left\|\hat{\boldsymbol{z}}^h_{k+1|k}\right\| \le \bar{z}_h$. With $p_{\max} = \lambda_{\max}(P)$, the Cauchy–Schwarz inequality gives

$$\Delta V_k \le \Delta V^h_k + 2\|P\|\bar{z}_h\bar{r} + p_{\max}\bar{r}^2 \tag{24}$$

Define $\beta_h = 2\|P\|\bar{z}_h\bar{r} + p_{\max}\bar{r}^2$. In a no-event period, Equation (19) directly yields the actual descent bound:

$$\Delta V_k \le -\alpha\|\boldsymbol{z}_k\|^2 + \delta_k + \beta_h \tag{25}$$

Adaptive Threshold Design

To vary trigger sensitivity with operating conditions, choose $c_i, c_\omega, c_s \ge 0$, define the electrical-speed reference $\omega^*_e = p_n\omega^*_m$ and normalization base $\omega_N > 0$, and construct the dimensionless operating indicator

$$\chi_k = \frac{c_i\|\boldsymbol{z}_k\|}{I_N} + \frac{c_\omega|\omega^*_e - \hat{\omega}_e|}{\omega_N} + \frac{c_s\|\boldsymbol{s}_k\|}{I_N} \tag{26}$$

$$\delta^{\mathrm{tar}}_k = \delta_{\min} + \frac{\delta_{\max} - \delta_{\min}}{1 + \gamma\chi_k} \tag{27}$$

$$\delta_{k+1} = \mathrm{Proj}_{[\delta_{\min},\delta_{\max}]}\{\rho\delta_k + (1-\rho)\delta^{\mathrm{tar}}_k\} \tag{28}$$

Here, $\gamma > 0$, $0 \le \rho < 1$, $0 \le \delta_{\min} \le \delta_{\max}$, and $\delta_0 \in [\delta_{\min}, \delta_{\max}]$. Equation (26) permits current-error, speed-error, and observer-residual terms. In the simulations and experiments reported here, $c_i = c_\omega = 0$, so threshold adaptation is driven solely by the observer residual; the compensated-current error remains part of the descent test.

Equation (27) shows that a larger χ_k reduces the target threshold. First-order smoothing and interval projection keep $\delta_k \in [\delta_{\min}, \delta_{\max}]$. A rising residual tightens the test and causes more re-enumerations; a falling residual relaxes it and allows longer vector holds. In tuning, $\delta_{\min}$ sets the accuracy requirement under high uncertainty, while $\delta_{\max}$ sets the allowed update reduction and ultimate bound. The parameters γ and ρ control residual sensitivity and threshold smoothing. The hold limit $N_{\max}$ is applied last.

To establish a descent certificate for the event branch and clarify the constants in Assumption 3, define the following quantities for any feasible candidate $\boldsymbol{v} \in \mathcal{U}_f(k)$:

$$\hat{\boldsymbol{z}}_{k+1|k}(\boldsymbol{v}) = A_{k+1}\hat{\boldsymbol{x}}_{k+1|k} + B\boldsymbol{v} + \boldsymbol{c}_{k+1} - \boldsymbol{x}^*_{k+2}, \qquad \Delta\hat{V}_k(\boldsymbol{v}) = V\Big(\hat{\boldsymbol{z}}_{k+1|k}(\boldsymbol{v})\Big) - V(\boldsymbol{z}_k). \tag{29}$$

Let $R_k(\boldsymbol{v}) = \lambda_{\mathrm{sw}}\|S(\boldsymbol{v}) - S(\boldsymbol{u}_{k-1})\|_1 + J_c(\boldsymbol{v})$. When the cost-function weight satisfies $Q = P$, Equation (8) can be written as $J_k(\boldsymbol{v}) = \Delta\hat{V}_k(\boldsymbol{v}) + V(\boldsymbol{z}_k) + R_k(\boldsymbol{v})$. Optimality gives the following relation between nominal predicted increments:

$$\Delta\hat{V}_k(\boldsymbol{v}^*_k) \le \Delta\hat{V}_k(\boldsymbol{v}_{c,k}) + R_k(\boldsymbol{v}_{c,k}) - R_k(\boldsymbol{v}^*_k). \tag{30}$$

The next step relates this prediction-level inequality to the actual increment ΔV_k.

To construct an auxiliary comparison vector for the local analysis, choose a feedforward voltage $\boldsymbol{u}_{ff,k}$ satisfying the nominal reference model

$$\boldsymbol{x}^*_{k+2} = A_{k+1}\boldsymbol{x}^*_{k+1} + B\boldsymbol{u}_{ff,k} + \boldsymbol{c}_{k+1}, \tag{31}$$

and select an auxiliary analysis gain K such that the contraction condition in Assumption 3 holds over Ω_z. Set $\boldsymbol{u}_{c,k} = \boldsymbol{u}_{ff,k} - K\boldsymbol{z}_k$. This gain constructs the comparison vector used in the certificate; the implemented controller follows the finite-set law below. Project the comparison voltage onto the finite set of voltage vectors satisfying the one-step current constraint:

$$\boldsymbol{v}_{c,k} \in \underset{\boldsymbol{v}\in\mathcal{U}_f(k)}{\arg\min} \left\| B(\boldsymbol{v} - \boldsymbol{u}_{c,k}) \right\|_P^2, \qquad \boldsymbol{\varepsilon}_{p,k} = B(\boldsymbol{v}_{c,k} - \boldsymbol{u}_{c,k}). \tag{32}$$

With the nominal closed-loop error matrix $F_k = A_{k+1} - BK$, the reference model directly gives

$$\hat{\boldsymbol{z}}_{k+1|k}(\boldsymbol{v}_{c,k}) = F_k\boldsymbol{z}_k + \boldsymbol{\varepsilon}_{p,k}. \tag{33}$$

Assumption 3 (local descent condition)**.** *Within the compact local domain $\Omega_z = \{\boldsymbol{z} : V(\boldsymbol{z}) \le \bar{V}\}$, the feasible set $\mathcal{U}_f(k)$ is nonempty, and the periodic full-enumeration baseline and event test use the same weight $Q = P \succ 0$. There exist an auxiliary gain K, a nominal contraction margin $\alpha_0 > 0$, an actual descent coefficient $0 < \alpha < \min\{\alpha_0, \lambda_{\max}(P)\}$, a constant $\beta^* \ge 0$, and nonnegative constants c_p, c_o, c_w, c_R such that*

$$F_k^{\mathrm{T}} P F_k - P \preccurlyeq -\alpha_0 I_2, \qquad c_p \left\| \boldsymbol{\varepsilon}_{p,k} \right\|^2 + c_o \left\| \boldsymbol{\varepsilon}_{o,k} \right\|^2 + c_w \|\boldsymbol{w}_k\|^2 + c_R \le \beta^*. \tag{34}$$

Here, $\boldsymbol{\varepsilon}_{o,k}$ collects prediction mismatch from state observation and reference extrapolation, while $\boldsymbol{w}_k$ is the discrete-model disturbance. The actual compensated-error update is written as

$$\boldsymbol{z}^*_{k+1} = \hat{\boldsymbol{z}}_{k+1|k}(\boldsymbol{v}^*_k) + \boldsymbol{\varepsilon}_{o,k} + \boldsymbol{w}_k. \tag{35}$$

Because both $\boldsymbol{v}_{c,k}$ and $\boldsymbol{v}^*_k$ are feasible, their constraint penalties vanish. The Hamming distance across three inverter legs is at most 3, so $R_k(\boldsymbol{v}_{c,k}) - R_k(\boldsymbol{v}^*_k) \le c_{\mathrm{sw}}$, where $c_{\mathrm{sw}} = 3\lambda_{\mathrm{sw}}$. Substituting the preceding error relations into the quadratic increment, applying the optimality inequality, and absorbing cross terms by Young's inequality using the available margin $\alpha_0 - \alpha$ yields finite constants c_p, c_o, c_w, and c_R ($\ge c_{\mathrm{sw}}$). Assumption 3 combines this optimality relation with the local contraction condition. The condition can be certified pointwise or by interval bounds using A_k, B, P, K, and the error bounds.

Consequently, the actual one-step increment $\Delta V^*_k = V(\boldsymbol{z}^*_{k+1}) - V(\boldsymbol{z}_k)$ associated with the optimal vector after an event satisfies

$$\Delta V^*_k \le -\alpha\|\boldsymbol{z}_k\|^2 + c_p \left\| \boldsymbol{\varepsilon}_{p,k} \right\|^2 + c_o \left\| \boldsymbol{\varepsilon}_{o,k} \right\|^2 + c_w \|\boldsymbol{w}_k\|^2 + c_R. \tag{36}$$

Equation (36) follows from the complete local condition in Assumption 3. The simulations use $Q = P = I_2$ and enforce feasibility through the current constraint and zero-vector fallback.

To state a condition for positive invariance of the local domain, let $a = \alpha/\lambda_{\max}(P)$ and define

$$\bar{c} = \max\{\beta^*,\ \delta_{\max} + \beta_h\}. \tag{37}$$

Assumption 4. *The initial compensated-current error satisfies $\boldsymbol{z}_0 \in \Omega_z$. Within Ω_z, the prediction-error bound $\bar{r}$ and β_h are valid, and $\bar{c} \le a\bar{V}$. All held-vector predictions satisfy the hard current*

constraint, or re-enumeration is triggered before a potential violation. The feasible set is nonempty at every enumeration. The protective zero-vector fallback handles trajectories that reach the feasibility boundary.

Assumptions 3 and 4 formalize the local descent certificate and prediction-error bounds. The implementation enforces current-limit feasibility and maximum hold duration online, and the zero-vector fallback supplies the protective action.

Uniform Ultimate Boundedness of the Event-Triggered Closed Loop

The following result applies after the sliding error has entered the boundary layer of Theorem 1 and the PLL satisfies the local locking condition of Assumption 2. At that point, the observer-error bound $\bar{\varepsilon}_o$, prediction-error bound $\bar{r}$, and induced constant β_h are taken as uniform bounds valid over Ω_z and are used to verify the constants in Assumptions 3 and 4.

Theorem 2. *Under Assumptions 1–4, with the threshold updated by Equation (28) so that $\delta_k \in [\delta_{\min}, \delta_{\max}]$, the compensated-current error z_k is uniformly ultimately bounded and its Lyapunov sublevel set Ω_z is positively invariant. The Lyapunov function $V_k = V(z_k)$ satisfies the uniform difference inequality*

$$V_{k+1} - V_k \le -\alpha \|z_k\|^2 + \bar{c} \tag{38}$$

and the error satisfies the ultimate bound

$$\limsup_{k\to\infty} \|z_k\| \le \sqrt{\frac{\bar{c}\,\lambda_{\max}(P)}{\alpha \lambda_{\min}(P)}} \tag{39}$$

Proof. Consider the event and no-event branches. If $\Gamma_k = 1$, the candidates are enumerated and $\Delta V_k = \Delta V_k^*$. Assumption 3 and Equation (36) give $\Delta V_k \le -\alpha\|z_k\|^2 + \beta^*$. If $\Gamma_k = 0$, the no-event condition, Equation (25), and $\delta_k \le \delta_{\max}$ give $\Delta V_k \le -\alpha\|z_k\|^2 + \delta_{\max} + \beta_h$. Thus, both branches satisfy

$$\Delta V_k \le \begin{cases} -\alpha\|z_k\|^2 + \beta^*, & \Gamma_k = 1, \\ -\alpha\|z_k\|^2 + \delta_k + \beta_h, & \Gamma_k = 0 \end{cases} \le -\alpha\|z_k\|^2 + \bar{c}. \tag{40}$$

Since $V_k = z_k^{\mathrm{T}} P z_k \le \lambda_{\max}(P)\|z_k\|^2$, it follows that $\|z_k\|^2 \ge V_k/\lambda_{\max}(P)$. Substituting this into Equation (38) yields

$$V_{k+1} \le \left(1 - \frac{\alpha}{\lambda_{\max}(P)}\right) V_k + \bar{c} \tag{41}$$

Assumption 3 implies $0 < a < 1$. To establish positive invariance of Ω_z, suppose $V_k \le \bar{V}$. By $\bar{c} \le a\bar{V}$ in Assumption 4, $V_{k+1} \le (1-a)\bar{V} + \bar{c} \le \bar{V}$. Since $V_0 \le \bar{V}$, induction gives $V_k \le \bar{V}$ for all k, so the local bounds used above remain valid throughout the proof. Expanding Equation (41) recursively gives

$$V_k \le (1-a)^k V_0 + \frac{\bar{c}}{a}\left[1 - (1-a)^k\right] \tag{42}$$

As $k \to \infty$, $\limsup_{k\to\infty} V_k \le \bar{c}/a = \bar{c}\lambda_{\max}(P)/\alpha$. Combining this with $V_k \ge \lambda_{\min}(P)\|z_k\|^2$ proves Equation (39). □

The bound shows that a larger $\delta_{\max}$ can reduce re-optimization but may enlarge the ultimate bound. Observer error affects both the prediction error of the hold branch and the descent margin of the enumeration branch. A rising residual tightens the threshold and

increases re-enumeration; a falling residual allows longer vector holds. Theorem 2 gives a local uniform-ultimate-bound result for the compensated-current error under the stated operating conditions.

3. Results

3.1. Simulation Results

3.1.1. Simulation Parameters and Comparison Groups

The simulations use the nominal parameters of a 100 W-class surface-mounted PMSM, listed in Table 2. Predicted current and its limit are expressed as peak values, with normalization base and predicted-current ceiling $I_b = I_{\max} = 7.8$ A. Figures 3 and 4 cover 0.40 s, whereas Figures 5–7 cover 0.60 s. The power-stage simulation step is 1 µs.

Table 2. Main PMSM and control-system parameters.

Parameter	Value	Parameter	Value
Rated power, P_N	100 W	DC-bus voltage, V_{dc}	24 V
Rated phase current, I_{rated}	5.5 A	Rated speed, n_N	3000 r/min
Rated torque, T_N	0.32 N m	Pole-pair number, p_n	4
Stator resistance, R_s	0.65 Ω/phase	d- and q-axis inductances, $L_d = L_q$	0.45 mH
PM flux linkage, ψ_f	0.0070 Wb	Equivalent inertia, J_{eq}	2.0×10^{-5} kg m^2
Viscous damping, B_m	2.0×10^{-5} N m s/rad	Control period, T_s	10 µs

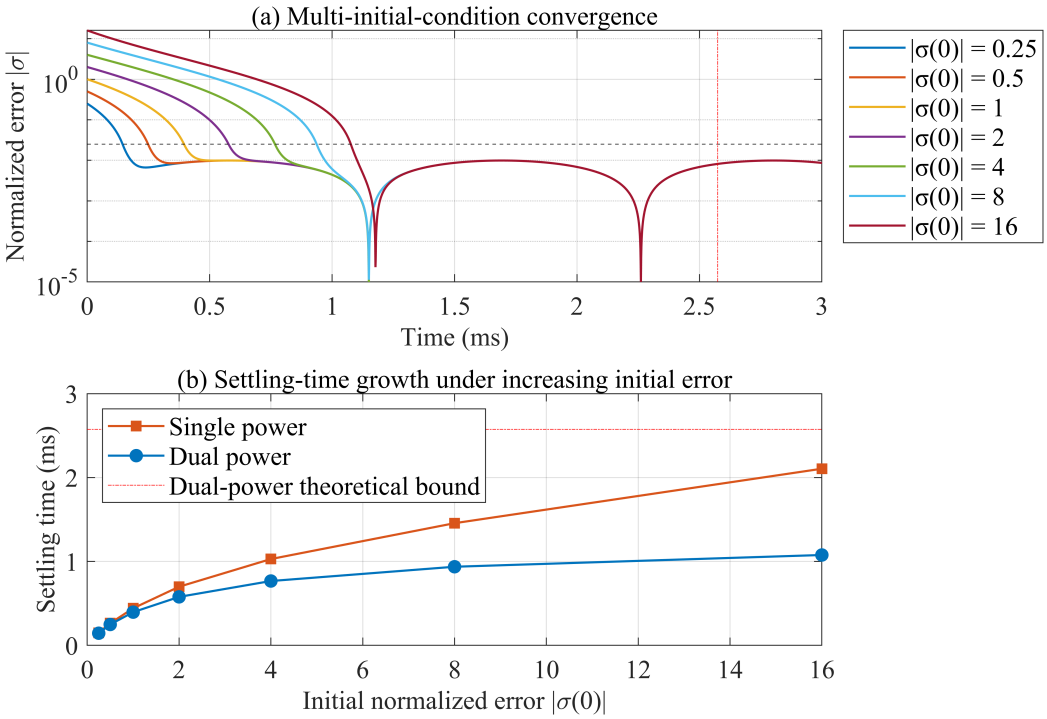


Figure 3. Practical fixed-time convergence of the double-power saturated reaching law. The horizontal dashed line denotes the boundary layer, and the red dash–dot line denotes the theoretical bound.

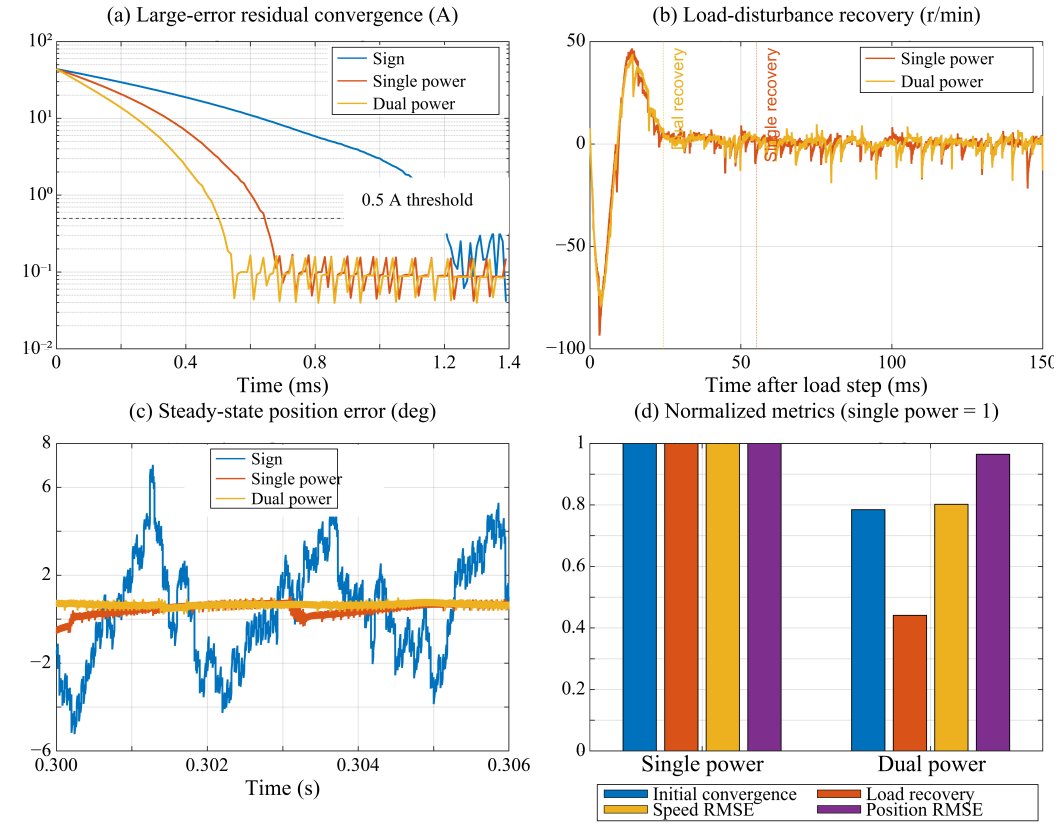


Figure 4. Large-error convergence, disturbance recovery, and steady-state accuracy for different SMO reaching laws.

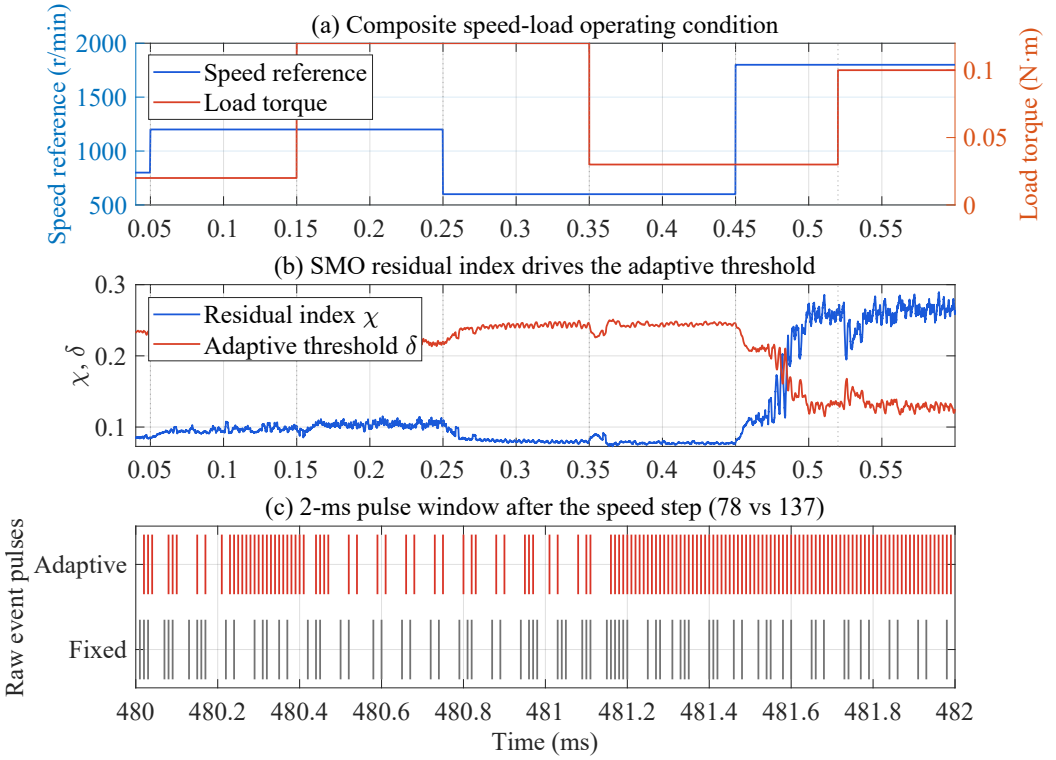


Figure 5. Observer-residual-driven threshold adaptation and transient trigger activity.

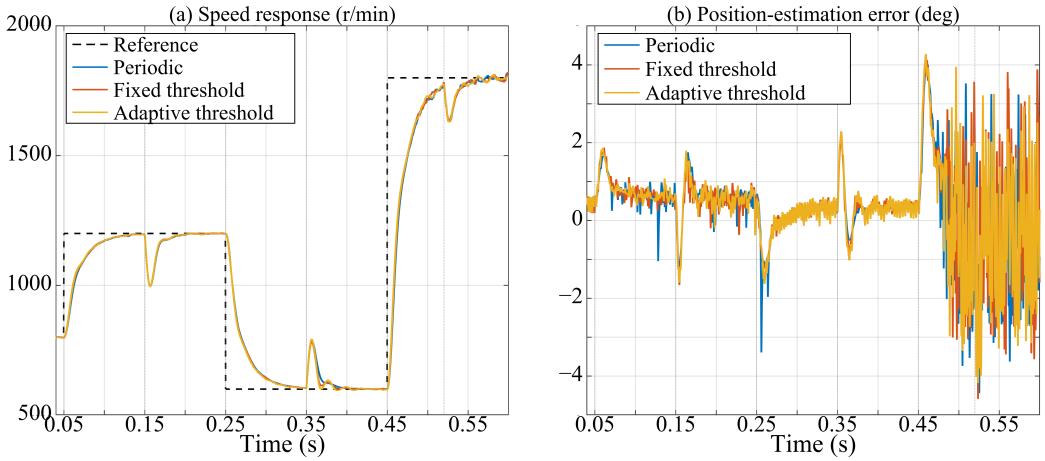


Figure 6. Control performance under periodic, fixed-threshold, and adaptive-threshold updates.

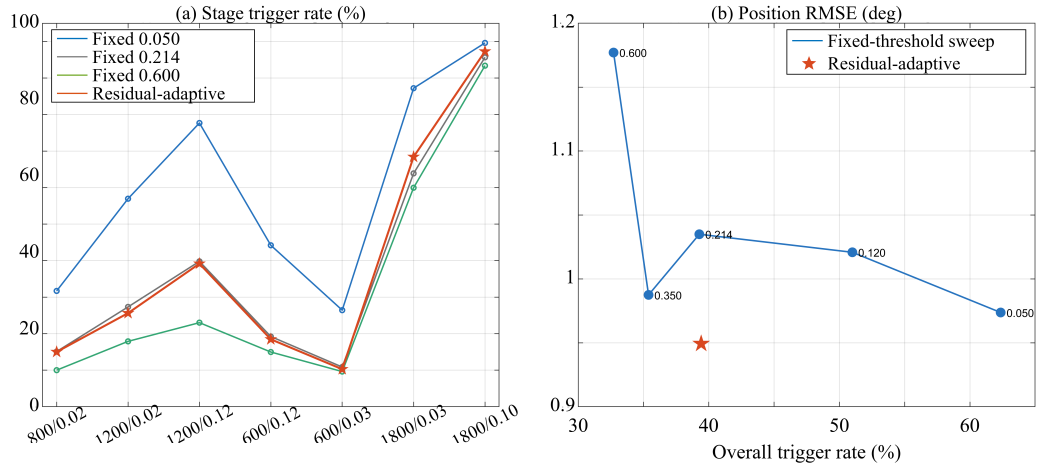


Figure 7. Performance–update-budget relationship for fixed-threshold sweeps and residual-adaptive triggering. In (**b**), the red star denotes the residual-adaptive result.

The speed PI gains are $K_p = 0.14$ and $K_i = 9$. The q-axis current-reference slew-rate limit is 2200 A/s, and the speed-command time constant is 22 ms. The back-EMF low-pass-filter time constant is 30 µs, with PLL gains $K_{p,\mathrm{PLL}} = 1450$ and $K_{i,\mathrm{PLL}} = 5.25 \times 10^5$. The observer uses $k_0 = 1.8\psi_f \max(|\hat{\omega}_e|, 100)/L_s + 3000$ A/s, $k_1 = 25000$ A/s, $k_2 = 8000$ A/s, $p = 0.5$, $q = 1.5$, and $\varphi = 0.025$. At the minimum scheduled speed, $k_0 = 5800$ A/s and the Assumption 1 disturbance envelope is 4556 A/s, leaving a gain margin of 1244 A/s, or 159.5 s^{-1} after normalization.

The base event-strategy parameters are $\alpha = 0.003$, $\delta_{\min} = 0.015$, $\delta_{\max} = 0.300$, $\gamma = 8$, $\rho = 0.97$, $N_{\max} = 40$, and $\lambda_{\mathrm{sw}} = 0.012$. For the composite profile in Figures 5–7, $c_i = c_\omega = 0$, $c_s = 8$, $\delta_{\min} = 0.030$, $\delta_{\max} = 0.650$, and $\gamma = 25$. The fixed-threshold baseline in Figures 5 and 6 uses $\delta_{\mathrm{fix}} = 0.214$; Figure 7 additionally sweeps $\delta_{\mathrm{fix}} = 0.050$, 0.120, 0.214, 0.350, and 0.600. All adaptive groups use only the residual term, namely, $\chi_k = 8\|s_k\|/I_b$.

Five comparison groups isolate the two design components: (A) periodic FCS-MPC with a sign-law SMO; (B) periodic FCS-MPC with a single-power saturated SMO; (C) periodic FCS-MPC with the double-power saturated SMO; (D) fixed-threshold event-triggered FCS-MPC with the double-power saturated SMO; and (E) adaptive-threshold event-triggered FCS-MPC with the double-power saturated SMO. Groups A–C compare reaching laws, and groups C–E compare update strategies. Groups B and C share k_0, k_1, φ, injection limits, and filter settings; only group B sets $k_2 = 0$. Figure 4 also uses

$\hat{i}_\alpha(0) = 4I_b$ and $\hat{i}_\beta(0) = -4I_b$ to test capture from an initial observer offset far beyond normal operating errors.

3.1.2. Local Parameter Sensitivity

Each key parameter was varied individually about its nominal value while all others were fixed. Electrical-angle RMSE, speed-estimation RMSE during the 30 ms post-transition windows, and trigger rate were recorded, and Table 3 reports the change from the nominal case. All 13 cases remained stable: angle-RMSE changed by -6.9% to $+5.8\%$, and transient error by -0.6% to $+5.6\%$. The $\delta_{\max}$ sweep produced the largest change in trigger rate. This sensitivity is consistent with Equations (27) and (28), which give the instantaneous threshold response for a fixed residual, whereas the table averages the closed-loop response over the complete profile. Changing one parameter also changes the residual and the subsequent sequence of held vectors and events. The nominal set gives a practical balance among angle accuracy, transient speed estimation, and update activity.

Table 3. Closed-loop one-at-a-time local sensitivity relative to the nominal case.

Parameter	Low/Nominal/High	Δ Angle RMSE, L/H (%)	Δ Transient RMSE, L/H (%)	Δ Trigger Rate, L/H (%)
k_1 (kA/s)	20/25/30	$-1.3/-2.5$	$+4.0/+1.2$	$-0.2/+4.3$
k_2 (kA/s)	6.4/8.0/9.6	$-1.2/+0.7$	$+1.5/+1.5$	$+2.9/+0.9$
φ	0.020/0.025/0.030	$+3.5/+1.8$	$+4.0/+2.8$	$+9.8/-9.1$
γ	20/25/30	$+2.6/-5.7$	$+3.4/+5.1$	$+9.0/-13.5$
ρ	0.95/0.97/0.99	$+1.5/+0.3$	$-0.6/+0.5$	$+1.8/+2.8$
$\delta_{\max}$	0.52/0.65/0.78	$-6.9/+5.8$	$+5.6/+2.3$	$-24.1/+6.5$

3.1.3. Simulation Profile and Performance Measures

Figures 5–7 use a composite speed–load profile to assess the allocation of control updates across operating stages. The commanded speed is 800 r/min over 0–0.05 s, 1200 r/min over 0.05–0.25 s, 600 r/min over 0.25–0.45 s, and 1800 r/min over 0.45–0.60 s. The load torque is 0.02 N m over 0–0.15 s, 0.12 N m over 0.15–0.35 s, 0.03 N m over 0.35–0.52 s, and 0.10 N m over 0.52–0.60 s. Statistics begin at 0.04 s. The 30 ms following each operating-point transition forms a transient window; the remainder of the evaluation interval is treated as quasi-steady. All groups use identical reference trajectories, load sequences, initial estimation errors, and sampling settings. The controller and event condition are evaluated every 10 µs.

Figure 3 shows how the reaching time changes with the initial error. All trajectories in Figure 3a enter the $\varphi = 0.025$ boundary layer. As $|\sigma(0)|$ rises from 0.25 to 16, Figure 3b shows a progressively smaller increase in reaching time. At $|\sigma(0)| = 16$, the single-power law reaches the layer in about 2.11 ms and the double-power law in 1.08 ms, a 48.8% reduction. Direct substitution in Equation (13) gives 2.48 ms. The plotted 2.57 ms line uses the looser, φ-independent inequality $1 - \varphi^{1-p} \leq 1$, and every double-power case remains below it. The higher-power term dominates far from the sliding surface, while the lower-power term retains corrective action near the boundary layer.

Figure 4 changes only the SMO reaching law in the complete motor model. The double-power residual in Figure 4a enters the 0.5 A band at 0.51 ms; the single-power residual takes 0.65 ms. After the load step in Figure 4b, speed-estimation recovery falls from 55.23 to 24.35 ms. Continuous saturated injection also narrows the steady-state position-error band compared with sign injection. With the same saturation structure, the double-power law reduces speed RMSE from 3.464 to 2.779 r/min and position RMSE from 0.658° to 0.635° after 0.30 s. Figure 4d summarizes the four measures.

Figure 5 follows the residual, threshold, and event sequence over the same speed–load profile. During steady intervals, χ_k stays low and δ_k remains relaxed. After 0.45 s, the higher speed and load raise χ_k and tighten δ_k, so full enumeration occurs more often. Figure 5c enlarges the interval from 0.480 to 0.482 s. Of the 200 control samples, the adaptive group triggers 137 times and the fixed-threshold group 78 times. Figure 7 compares this redistribution over all operating stages.

Figure 6 compares speed response and position-estimation error over the 0.60 s composite profile. Across the three strategies, the speed trajectories remain close after each speed and load transition. The fixed- and adaptive-threshold cases also retain oscillation levels and position-error envelopes comparable to periodic updating. Figure 7 then quantifies how position accuracy varies with the update budget.

Figure 7a compares stage trigger rates for fixed thresholds and the adaptive rule. At 600 r/min and 0.03 N m, the $\delta_{\text{fix}} = 0.050$ group triggers in 26.43% of periods, compared with 10.27% for the adaptive group. Figure 7b gives a budget-matched comparison: $\delta_{\text{fix}} = 0.214$ and the adaptive rule have overall trigger rates of 39.28% and 39.42%, while their quasi-steady position RMSE values are 1.035° and 0.949°. At high speed and heavy load, $\delta_{\text{fix}} = 0.600$ and the adaptive rule trigger at 93.38% and 97.29%; their position RMSE values are 2.071° and 1.861°.

The simulation logs contain about 448,000 full-enumeration candidate-state checks for periodic control, 176,000 for the fixed threshold, and 177,000 for the adaptive rule. Relative to periodic control, the adaptive rule cuts full-search checks by 60.6%. Counting one held-vector prediction in each of the $N = 56{,}000$ periods gives 232,600 branch-level prediction evaluations for the adaptive method and 448,000 for periodic enumeration, a 48.1% reduction.

3.2. Experimental Validation

The platform in Figure 8 comprises a PMSM, a magnetic-powder brake, a torque–speed sensor, a three-phase inverter, a real-time controller, and a host computer. The host computer generates the control code and downloads it to the DSP–FPGA controller. The controller drives the inverter, the brake applies load torque, and the host records the waveforms. The logged signals include speed, current, estimated electrical angle, and event activity. Controller execution time was measured by toggling a DSP GPIO at branch entry and exit and recording the pulse width with an oscilloscope. Periodic and residual-adaptive FCS-MPC use the same double-power saturated SMO and PLL. The encoder is used only as the reference for evaluating the sensorless position estimate. Figures 4–7 test the individual components, while the hardware experiment tests the complete controller.

The speed command rises from 1200 to 1500 r/min at 0.15 s, and load torque rises from 0.02 to 0.10 N m at 0.35 s. Periodic control enumerates all candidate vectors at every sample. The adaptive controller uses the observer residual to adjust its trigger threshold. Both groups use the same observer-update rate, reference trajectory, and load conditions. Event-triggered operation begins after PLL locking, and loss of lock returns the controller to periodic enumeration. The hardware profile contains one speed transition and one load step; Figures 4–7 provide the corresponding controlled component tests.

In Figure 9a, both strategies track the 1200-to-1500 r/min speed step smoothly and recover toward the command after the load increase. Their trajectories remain close during acceleration and disturbance recovery. Figure 9c shows the α-axis current before and after loading: current amplitude rises with the increased load, and both groups show closely matched amplitude and phase changes during vector holding.

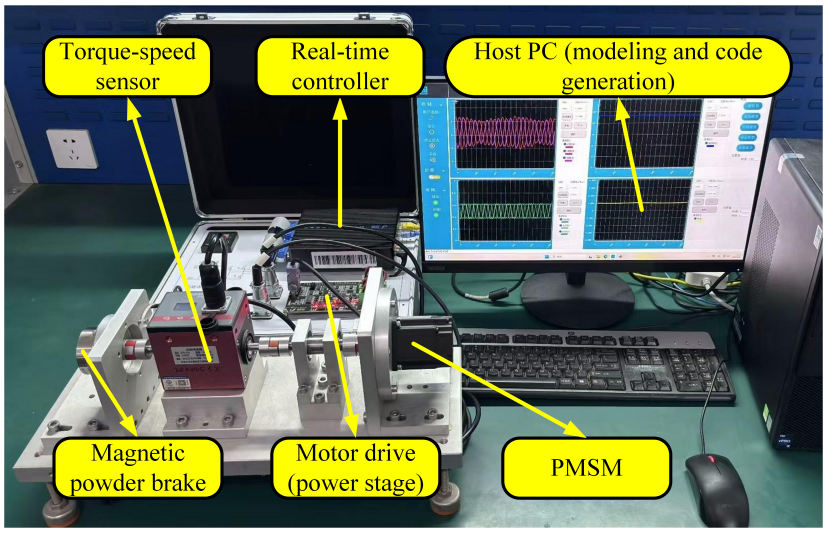


Figure 8. PMSM experimental platform based on automatic code generation.

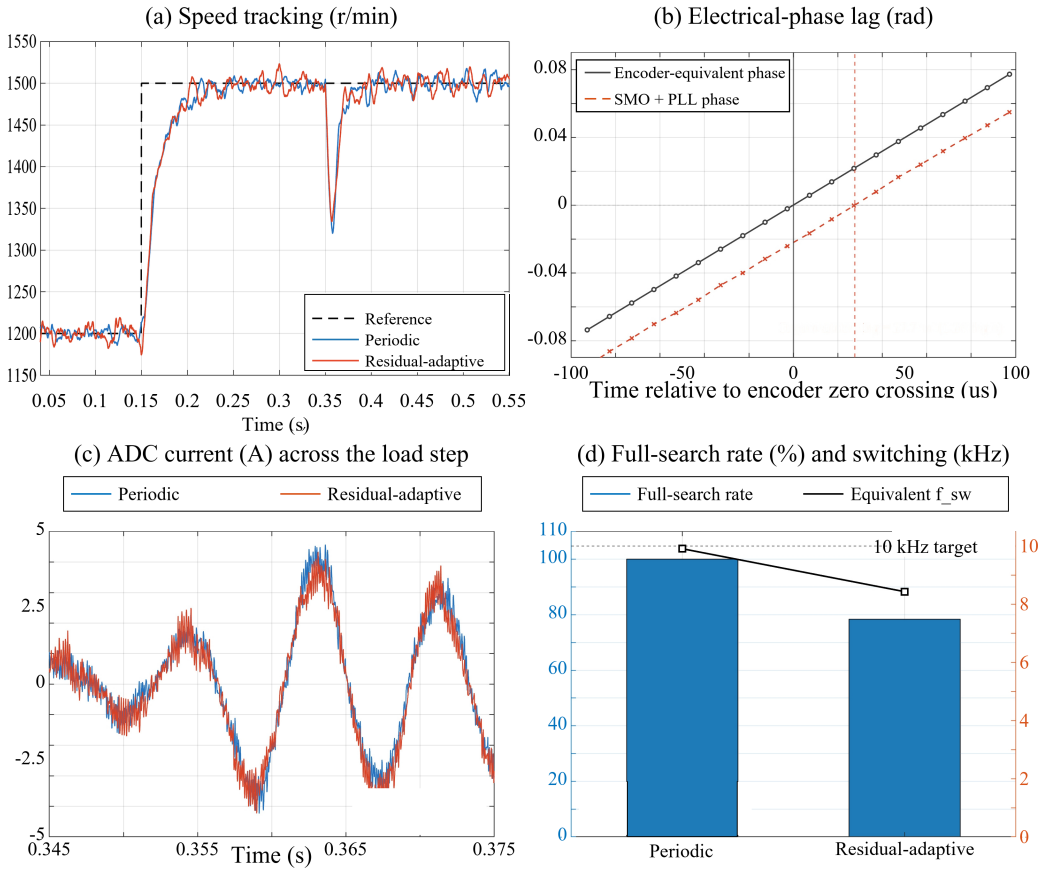


Figure 9. Experimental results under speed and load steps: (**a**) speed tracking; (**b**) local electrical-angle lag, where the vertical dotted line marks the SMO+PLL zero crossing and its offset from the encoder zero crossing at 0 μs gives the measured lag; (**c**) α-axis current before and after the load step; and (**d**) FCS-MPC full-search rate and equivalent switching frequency.

Figure 9b shows local electrical-angle tracking. The reference phase and SMO–PLL estimate are sampled every 10 µs and connected by straight lines; red crosses mark estimated samples. Zero-crossing instants are obtained by linear interpolation between adjacent samples. In the representative positive-lag window shown, the two phase curves have similar slopes and the estimated phase lags by about 27.7 µs, corresponding to approximately 1.0°

electrical. This local zero-crossing comparison complements the electrical-angle RMSE over the full evaluation interval in Table 4.

Table 4. Experimental control performance and update activity under speed and load steps.

Measure	Periodic	Residual-Adaptive	Difference	Interpretation
Full-search rate (%)	100.00	78.38	−21.6%	Periods with full enumeration
Prediction evaluations incl. held-vector checks (10^4)	40.80	37.08	−3.72	Non-reuse branch-level count
Branch execution time (µs)	7.9	3.1 (hold) 8.7 (trigger)	–	Measured control paths
Mean execution time (µs)	7.9	7.5	−0.4	Weighted by full-search rate
Equivalent switching frequency (kHz)	9.91	8.43	−1.48	Average device switching activity
Speed-tracking RMSE (r/min)	11.07	12.29	+1.22	Speed-tracking error
Electrical-angle RMSE (°)	1.731	2.131	+0.400	Position-estimation error

Note: The evaluation interval is 0.04–0.55 s. RMSE is calculated from the original discrete samples; smaller values indicate smaller errors. The adaptive mean execution time is weighted by the observed full-search rate. Differences are residual-adaptive values minus periodic values and use the units given in the Measure column.

Figure 9d and Table 4 report control accuracy and update activity. The full-search rate is the fraction of periods in which all eight vectors are enumerated. The equivalent switching frequency is the number of three-leg switching-state transitions divided by six times the evaluation interval. The adaptive controller has a full-search rate of 78.38%, and full-enumeration checks fall from 408,000 to 319,800 (21.6%). Adding one held-vector prediction in each of the 51,000 periods gives 370,800 branch-level prediction evaluations, 9.1% fewer than periodic enumeration. The measured execution times are 7.9 µs for periodic enumeration, 3.1 µs for the holding branch, and 8.7 µs for the triggered full search. The worst measured branch remains within the 10 µs control period. At the observed full-search rate, the weighted adaptive mean is 7.5 µs. Equivalent switching frequency falls from 9.91 to 8.43 kHz. Speed RMSE rises from 11.07 to 12.29 r/min, and electrical-angle RMSE from 1.731° to 2.131°.

The hardware test uses $\delta_{\min} = 0.015$, $\delta_{\max} = 0.300$, $\gamma = 8$, and $\rho = 0.97$. Its threshold bounds are tighter than the composite-simulation values of 0.030 and 0.650, which makes the held-vector descent test more selective and contributes to the measured full-search rate of 78.38%. Mean execution time falls by 0.4 µs, while speed and angle RMSE increase by 1.22 r/min and 0.400°.

4. Discussion

Figures 3 and 4 isolate the reaching law, while Figures 5–7 isolate the update rule. Groups A–C differ in the reaching law; Groups C–E differ in the update strategy. Figure 7 also compares the fixed and adaptive rules at nearly equal trigger rates. With $\delta_{\text{fix}} = 0.350$, the fixed-threshold group has a trigger rate of 35.39%, speed RMSE of 40.57 r/min, and step recovery time of 102.20 ms. The adaptive values are 39.42%, 42.16 r/min, and 103.65 ms. At the closer trigger-rate match in Figure 7, the adaptive rule lowers position RMSE from 1.035° to 0.949°. On the hardware profile, its measured mean execution time is 7.5 µs, compared with 7.9 µs for periodic enumeration. Future work will extend the matched-budget hardware comparison to more operating conditions. Figure 3 uses a scalar comparison system; Figures 4–7 use the nominal motor parameters in Table 2. The implementation monitors PLL locking, current feasibility, and hold duration online.

The closest published methods save computation in other ways. Ref. [6] reduces the work inside each predictive update. Ref. [30] uses a model-derived event condition and an SMO for load-torque compensation. Refs. [7,16] improve the sensorless model through parameter correction or identification. Here, the observer residual determines when the next candidate search is needed. The simulations cut candidate-state checks by 60.6% and give lower position RMSE at a similar trigger rate; the hardware test also records fewer full searches and a lower switching frequency.

5. Conclusions

This study set out to let the observer residual decide when a new candidate search is needed, and the simulations and bench tests confirm that this is achievable at a measurable accuracy cost. At the largest tested initial error, the double-power law shortens boundary-layer entrance from 2.11 to 1.08 ms and post-load recovery from 55.23 to 24.35 ms. The adaptive rule cuts simulated candidate checks by 60.6% and lowers position RMSE from 1.035° to 0.949° at a similar update rate. On the hardware bench, full-enumeration checks and switching frequency fall by 21.6% and 14.9%; speed and angle RMSE increase by 1.22 r/min and 0.400°, respectively. For low-voltage auxiliary drives with a 10 µs control period, the scheme offers a way to trade switching activity against angle accuracy without added hardware. Future work will study automatic tuning, low-speed polarity detection, and matched-budget tests over a wider set of operating conditions.

Author Contributions: Conceptualization, Z.X.; methodology, Z.X. and Y.W.; formal analysis, Z.X.; investigation, Z.X. and H.Z.; data curation, Z.X.; writing—original draft preparation, Z.X.; writing—review and editing, X.M., Y.W., P.F., H.Z., and Y.G.; supervision, X.M.; project administration, X.M.; funding acquisition, X.M.; validation, P.F.; resources, P.F. and Y.G.; project coordination, Y.G. All authors have read and agreed to the published version of the manuscript.

Funding: This work was supported by the Project of National Natural Science Foundation of China (No. 52672468) and partly supported by the 2025 Songjiang District Science and Technology Key Project (No. 2025SJJBGS3) and the 2026 Songjiang District Industry–University–Research Cooperation Project (No. 2026-02).

Data Availability Statement: The data supporting the findings of this study are included in the article. Further inquiries can be directed to the corresponding author.

Acknowledgments: During the preparation of this work, the authors used an AI-based tool for English polishing and assistance with LaTeX typesetting. The authors reviewed and edited the output and take full responsibility for the content of the published article.

Conflicts of Interest: Yang Gao is an employee of Shanghai Kehai Huatai Marine Electrical Co., Ltd. The company had no role in the design of the study; in the collection, analysis, or interpretation of data; in the writing of the manuscript; or in the decision to publish the results. The remaining authors declare that the research was conducted in the absence of any commercial or financial relationships that could be construed as potential conflicts of interest.

References

1. Kouro, S.; Cortes, P.; Vargas, R.; Ammann, U.; Rodriguez, J. Model Predictive Control—A Simple and Powerful Method to Control Power Converters. *IEEE Trans. Ind. Electron.* **2009**, *56*, 1826–1838. https://doi.org/10.1109/TIE.2008.2008349.
2. Li, T.; Sun, X.; Lei, G.; Yang, Z.; Guo, Y.; Zhu, J. Finite-Control-Set Model Predictive Control of Permanent Magnet Synchronous Motor Drive Systems—An Overview. *IEEE/CAA J. Autom. Sin.* **2022**, *9*, 2087–2105. https://doi.org/10.1109/JAS.2022.105851.
3. Rodriguez, J.; Kazmierkowski, M.P.; Espinoza, J.R.; Zanchetta, P.; Abu-Rub, H.; Young, H.A.; Rojas, C.A. State of the Art of Finite Control Set Model Predictive Control in Power Electronics. *IEEE Trans. Ind. Inform.* **2013**, *9*, 1003–1016. https://doi.org/10.1109/TII.2012.2221469.
4. Zhang, X.; Yu, X.; Zhang, G. Adaptive Model Predictive Current Control for PMSM Drives Based on Bayesian Inference. *IEEE Trans. Power Electron.* **2025**, *40*, 8490–8502. https://doi.org/10.1109/TPEL.2025.3535907.

5. Wang, J.; Liu, Y.; Yang, J.; Wang, F.; Rodriguez, J. Adaptive Integral Extended State Observer-Based Improved Multistep FCS-MPCC for PMSM. *IEEE Trans. Power Electron.* **2023**, *38*, 11260–11276. https://doi.org/10.1109/TPEL.2023.3279856.
6. Sun, J.; Yang, Y.; Hu, J.; Zhang, X.; Li, X.; Rodriguez, J. A Novel Model Predictive Current Control with Reduced Computational Burden Based on Discrete Space Vector Modulation for PMSM Drives. *CPSS Trans. Power Electron. Appl.* **2024**, *9*, 292–303. https://doi.org/10.24295/CPSSTPEA.2024.00009.
7. Zhou, R.; Wang, H. Model Predictive Speed and Voltage Control of Sensorless PMSM with Parameter Rectification and a Reduced-Order EKF. *IEEE Trans. Ind. Electron.* **2026**, *early access*. https://doi.org/10.1109/TIE.2026.3695118.
8. Zhao, M.; Zhang, S.; Zhang, C.; Li, X.; Dong, Y. A Parameter Robust Finite Control Set Model Predictive Current Control Based on Incremental Prediction Model for SPMSM Drives. *IEEE J. Emerg. Sel. Top. Ind. Electron.* **2024**, *5*, 1292–1302. https://doi.org/10.1109/JESTIE.2024.3356976.
9. Zhang, Y.; Jin, J.; Huang, L. Model-Free Predictive Current Control of PMSM Drives Based on Extended State Observer Using Ultralocal Model. *IEEE Trans. Ind. Electron.* **2021**, *68*, 993–1003. https://doi.org/10.1109/TIE.2020.2970660.
10. Chen, L.; Jin, Z.; Shao, K.; Wang, H.; Wang, G.; Iu, H.H.C.; Fernando, T. Sensorless Fixed-Time Sliding Mode Control of PMSM Based on Barrier Function Adaptive Super-Twisting Observer. *IEEE Trans. Power Electron.* **2024**, *39*, 3037–3051. https://doi.org/10.1109/TPEL.2023.3336743.
11. Chen, Y.; Yang, T.; Fan, L.; Bozhko, S. Sensorless Control Design of High-Speed Electric Drives in Discrete-Time Domain for Mild-Hybrid Turboprop Aircraft Applications. *IEEE Trans. Transp. Electrif.* **2023**, *9*, 3601–3619. https://doi.org/10.1109/TTE.2022.3206718.
12. Sreejith, R.; Singh, B. Sensorless Predictive Current Control of PMSM EV Drive Using DSOGI-FLL Based Sliding Mode Observer. *IEEE Trans. Ind. Electron.* **2021**, *68*, 5537–5547. https://doi.org/10.1109/TIE.2020.2996159.
13. Ge, Y.; Song, W.; Yang, Y.; Wheeler, P. A Polar-Coordinate-Multisignal-Flux-Observer-Based PMSM Non-PLL Sensorless Control. *IEEE Trans. Power Electron.* **2023**, *38*, 10579–10583. https://doi.org/10.1109/TPEL.2023.3289095.
14. Benevieri, A.; Formentini, A.; Marchesoni, M.; Passalacqua, M.; Vaccaro, L. Sensorless Control with Switching Frequency Square Wave Voltage Injection for SPMSM with Low Rotor Magnetic Anisotropy. *IEEE Trans. Power Electron.* **2023**, *38*, 10060–10072. https://doi.org/10.1109/TPEL.2023.3270357.
15. Jin, D.; Liu, L.; Lin, Q.; Liang, D. Sensorless Control Strategy of PMSM with Disturbance Rejection Based on Adaptive Sliding Mode Control Law. *IEEE Trans. Transp. Electrif.* **2024**, *10*, 5424–5438. https://doi.org/10.1109/TTE.2023.3327144.
16. Yang, C.; Liu, W.; Song, B.; Chau, K.T. Signal-Injection-Free Online Identification of Temperature-Dependent Electrical Parameters for SPMSM Drives: An Alternating Dual-Adaline Approach. *IEEE Trans. Transp. Electrif.* **2026**, *12*, 8447–8463. https://doi.org/10.1109/TTE.2026.3696388.
17. Gao, W.; Hung, J.C. Variable Structure Control of Nonlinear Systems: A New Approach. *IEEE Trans. Ind. Electron.* **1993**, *40*, 45–55. https://doi.org/10.1109/41.184820.
18. Levant, A. Sliding Order and Sliding Accuracy in Sliding Mode Control. *Int. J. Control* **1993**, *58*, 1247–1263. https://doi.org/10.1080/00207179308923053.
19. Yu, X.; Feng, Y.; Man, Z. Terminal Sliding Mode Control—An Overview. *IEEE Open J. Ind. Electron. Soc.* **2021**, *2*, 36–52. https://doi.org/10.1109/OJIES.2020.3040412.
20. Hou, Q.; Ding, S. Finite-Time Extended State Observer-Based Super-Twisting Sliding Mode Controller for PMSM Drives with Inertia Identification. *IEEE Trans. Transp. Electrif.* **2022**, *8*, 1918–1929. https://doi.org/10.1109/TTE.2021.3123646.
21. Polyakov, A. Nonlinear Feedback Design for Fixed-Time Stabilization of Linear Control Systems. *IEEE Trans. Autom. Control* **2012**, *57*, 2106–2110. https://doi.org/10.1109/TAC.2011.2179869.
22. Liu, Y.; Li, H.; Zuo, Z.; Li, X.; Lu, R. An Overview of Finite/Fixed-Time Control and Its Application in Engineering Systems. *IEEE/CAA J. Autom. Sin.* **2022**, *9*, 2106–2120. https://doi.org/10.1109/JAS.2022.105413.
23. Tabuada, P. Event-Triggered Real-Time Scheduling of Stabilizing Control Tasks. *IEEE Trans. Autom. Control* **2007**, *52*, 1680–1685. https://doi.org/10.1109/TAC.2007.904277.
24. Ge, X.; Han, Q.L.; Zhang, X.M.; Ding, D. Dynamic Event-Triggered Control and Estimation: A Survey. *Int. J. Autom. Comput.* **2021**, *18*, 857–886. https://doi.org/10.1007/s11633-021-1306-z.
25. Zhu, X.; Casau, P.; Silvestre, C. Model-Based Event-Triggered Control for Linear Systems Using a Finite-Time Convergent Observer. *Automatica* **2024**, *160*, 111458. https://doi.org/10.1016/j.automatica.2023.111458.
26. Heydari, R.; Farrokhi, M. Robust Event-Triggered Model Predictive Control of Polytopic LPV Systems: An Input-to-State Stability Approach. *Syst. Control Lett.* **2022**, *163*, 105202. https://doi.org/10.1016/j.sysconle.2022.105202.
27. Yang, Y.; Yao, X.; Xu, H. Disturbance-Observer-Based Event-Triggered Model Predictive Control of Nonlinear Input-Affine Systems. *Automatica* **2024**, *161*, 111504. https://doi.org/10.1016/j.automatica.2023.111504.
28. Wang, B.; Huang, J.; Wen, C.; Rodriguez, J.; Garcia, C.; Gooi, H.B.; Zeng, Z. Event-Triggered Model Predictive Control for Power Converters. *IEEE Trans. Ind. Electron.* **2021**, *68*, 715–720. https://doi.org/10.1109/TIE.2019.2962489.

29. Liu, X.; Qiu, L.; Wu, W.; Ma, J.; Fang, Y.; Peng, Z.; Wang, D.; Rodriguez, J. Event-Triggered ESO-Based Robust MPC for Power Converters. *IEEE Trans. Ind. Electron.* **2023**, *70*, 2144–2152. https://doi.org/10.1109/TIE.2022.3167135.
30. Shen, W.; Shao, L.; Liu, D.; Wang, J.; Ge, C. Event-Triggered FCS-MPC with Sliding Mode Observer for Permanent Magnet Synchronous Motor Servo Motion Systems. *IEEE Trans. Autom. Sci. Eng.* **2025**, *22*, 2257–2268. https://doi.org/10.1109/TASE.2024.3377639.
31. Bulut, M. Intelligent Controller Design for Electric Vehicle (EV) Speed Control Using an Inverse-Model-Based Reference-Model Learning Algorithm. *TechRxiv* **2024**. *preprint, version 2*. https://doi.org/10.36227/techrxiv.16783258.v2.

Disclaimer/Publisher's Note: The statements, opinions and data contained in all publications are solely those of the individual author(s) and contributor(s) and not of MDPI and/or the editor(s). MDPI and/or the editor(s) disclaim responsibility for any injury to people or property resulting from any ideas, methods, instructions or products referred to in the content.